Acta Astronautica 225 (2024) 27–40

Contents lists available at ScienceDirect

Acta Astronautica

journal homepage: www.elsevier.com/locate/actaastro

Research paper

HexSats: A novel flat hexagonal nanosatellite for high-power applications

Kash Saddul [*,1], James Saletes[1], Minkwan Kim[2], Alexander Wittig[2]

Department of Aeronautics and Astronautics, University of Southampton, University Road, Southampton, SO17 1BJ, Hampshire, United Kingdom

ARTICLE INFO

Keywords:
Flat satellite
Micro-thrust electric propulsion
Distributed propulsion
Very Low Earth Orbit
Satellite platform

ABSTRACT

We introduce the concept of HexSats, a 2.5 cm thick flat hexagonal satellite architecture, designed for efficient packing inside rocket fairings. For actuation, HexSats use a distributed micro-propulsion system (DμPS), consisting of arrays of small thrusters embedded in the satellite frame and producing thrust on the order of micro-Newtons. We investigate the HexSats' capability to operate at 250 km altitude in Very Low Earth Orbit (VLEO) with power requirements exceeding 100 W. Depending on the mission scenario, the HexSat can either constantly point in the Nadir direction or briefly track a target on the ground. The required angular acceleration and resulting drag profiles are analytically determined, along with the expected performance of the HexSats. These results are combined to examine the feasibility of the two mission profiles at different HexSat sizes and provide estimates of the power available to the payload at different VLEO altitudes. Our results show that a HexSat at 250 km can actively track up to 8 ground targets per orbit and provide over 100 W of average payload power in these scenarios.

1. Introduction

The popularity of the nanosatellite market, including CubeSats, stems from its low-cost approach to designing spacecraft [1]. Nowadays, with scientific advances constantly miniaturising electronics and other technologies, satellite operators can use nanosatellites to lower manufacturing and launch costs, without sacrificing performance. Standardised satellite form factors especially benefit from uniform launcher interfaces and predefined modular designs [2]. By minimising the design efforts and using Commercial-Off-The-Shelf (COTS) components, operators can minimise costs and accelerate the development time of a spacecraft. According to NASA's report on small satellite technology, the state-of-the-art of standardised satellite architectures are CubeSats and PocketCubes [3]. Both use a cubic form factor, with CubeSats having a base unit (1U) of a cube of 10 cm, while PocketCubes have a base unit (1P) of a 5 cm cube. Although they present similar features, CubeSats have been significantly more popular than PocketCubes, with the 3U-class being the most launched [4,5].

However, the standardisation of nanosatellites to a box-like structure has limited their surface area and power budgets. Many critical subsystems, such as attitude-orbit determination packages, solar arrays and optical sensors must be placed on the satellite's surface, typically leading to a significant integration challenge for the smaller range of nanosatellites. At the same time, the larger sizes typically still require deployable solar panels to meet the subsystems' power requirements [6,7]. As a result, nanosatellites have typically been ineligible for missions with wide aperture or high power requirements. This limitation has created interest in a new form factor capable of providing a high power and surface area while adhering to a standardised architecture to minimise costs and design efforts.

DiskSats are one such proposed form of spacecraft containerisation [8,9]. They are a thin, circular satellite form factor, initially created by The Aerospace Corporation as an alternative to CubeSats for applications presenting high power and aperture requirements. Supported by NASA, they now aim to create a new standard to provide a high-power-to-mass ratio platform that can be easily stacked in a launcher fairing [10]. Composed of a 1-meter diameter graphite facesheet with a 2.5-centimetre thick aluminium honeycomb core, each DiskSat provides a volume equivalent to a 20U CubeSat. Fig. 1 shows how a DiskSat compares to CubeSat and PocketQubes. A single unit provides a structural mass below 3 kg with enough surface area for over 200 W of peak power in ideal conditions, assuming the solar arrays fully cover one of the facesheets. The other facesheet would have the instruments mounted on it. The total launch weight of a DiskSat depends on the chosen launch vehicle's payload capacity. For instance, launching 20 DiskSats on RocketLab's Electron could allow individual DiskSats weighing up to 11 kg, including the payload. DiskSats sit on the boundary between two satellite class definitions, with a mass comparable to nanosatellites, and a size intuitively associated with

* Corresponding author.
E-mail address: kash.saddul@soton.ac.uk (K. Saddul).
[1] PhD candidate.
[2] Associate Professor.

https://doi.org/10.1016/j.actaastro.2024.09.007
Received 12 June 2024; Received in revised form 29 August 2024; Accepted 2 September 2024
Available online 4 September 2024

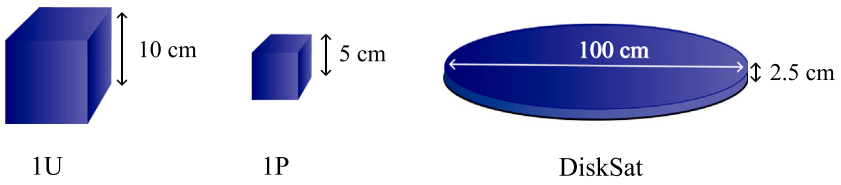

Fig. 1. Comparison of base units for a CubeSat (1U), a PocketQube (1P), and a DiskSat (not to scale).

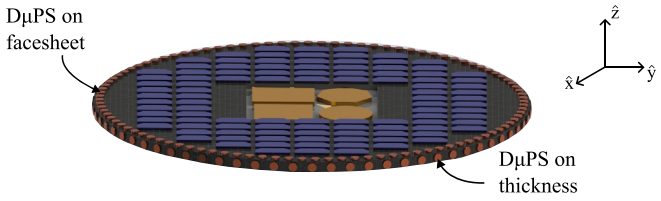

Fig. 2. Render of a DiskSat with the DμPS concept.

microsats. Their theoretical peak power-to-mass ratio would be around 18 W/kg, while typical 3U CubeSats, without deployables, have a theoretical peak power-to-mass ratio of 6 W/kg.

The Aerospace Corporation is preparing four DiskSats for in-orbit demonstration in 2024 to operate partly in Very Low Earth Orbit (VLEO) [11]. The proximity of the VLEO regime to the Earth's surface provides many benefits such as higher resolution and greater launch mass, as outlined in the work of Crisp et al. [12,13]. Similarly to CubeSats and PocketCubes, the demonstration DiskSats take advantage of existing COTS components available in the nanosatellite supply chain. However, the current market was primarily aimed at CubeSats, with their box-shaped form factor. Therefore, most COTS components are not made for the DiskSats' thin architecture. A notable example is the onboard electric propulsion (EP) system, Enpulsion's Nano-FEEP, a highly efficient Field Emission Electric Propulsion (FEEP) thruster that fits in the volume of a 1U CubeSat [14]. While DiskSats can easily cater to NanoFEEP's nominal power of 40 W, the dimensions of the thruster disrupt the thin, quasi-2D architecture of the satellite. The DiskSats will not only experience a higher drag, especially at lower altitudes, but their centres of mass will also be shifted, making attitude control more complex. The cube-like shape of the thruster also means that cut-outs are required in the disk, on the opposite side of the propulsion system, to allow for compact stacking in the launcher fairing.

The reason for this choice of propulsion system is the lack of a commercially available, flight-proven alternative on the market. While many electric propulsion systems can provide a similar thrust or power requirement, few existing architectures would have the dimensions required to maintain the thin form factor of the DiskSats. Of the 60 electric thrusters mentioned in NASA's report on small satellite technology, none have dimensions suitable for a thin form factor [3]. There is therefore a need for a miniature propulsion system capable of fitting in the thickness of the DiskSat while also providing meaningful manoeuvrability to the satellite.

Without commercially available flight-proven alternatives, we turn to emerging electric propulsion systems to provide appreciable impulse at small dimensions [15,16]. The following technologies show promising miniaturisation and are potentially suitable for the DiskSat platform.

Hall Effect Thrusters (HET) are the most popular type of EP [17]. However, efforts to downsize HETs have been challenging due to the higher surface-to-volume ratios in the ionisation chamber, and the resulting increased erosion rates have limited their operational lifetime [18]. Attempts to mitigate this issue often involve implementing magnetic shielding of the wall. However, this solution comes at the cost of complicating the magnetic circuitry, an already power-intensive subsystem [19]. Many experimental miniature thrusters have been developed, with few that could be considered for use on DiskSats. The Space Flight Laboratory in Canada has developed a HET with a 26 mm head capable of operating within the 50–200 W range [20]. An even lower power HET, presenting a 24 mm diameter and operating on 25 W, was developed by the Plasma Sources and Applications Centre/Space Propulsion Centre in Singapore [21]. Similarly, the TCHT-4, developed at the Osaka Institute of Technology in Japan, is a 7 × 14 mm cylindrical thruster that has a power range as low as 10 W, providing a specific impulse of 350 s [22]. Its peak efficiency occurs at 66 W with an Isp of 1580 s. According to Yeo et al. [19], only one miniature HET has successfully flown in Earth orbit, the ExoMG-nano [23]. Developed by Exotrail, it features an external tank measuring 3.5 cm, producing a thrust of 2 mN at a power of 53 W.

Gridded Ion Thrusters (GITs), an alternative form of electric propulsion, also present challenges in the miniaturisation process. According to the NASA Small Spacecraft Technology report, the smallest COTS GIT is the RIT-μX by Ariane Group, measuring 7.8 × 7.8 × 7.6 cm [3]. However, just like the nano-FEEP thruster, its dimensions still make it incompatible with the DiskSat's thin form factor. An experimental, miniaturised version of the RIT-μX, known as the RIT-2.5, was developed with a diameter of 25 mm [24]. This downsized thruster provides 575 μN of thrust at 34.4 W of power. Pennsylvania State University also studied a 25 mm ion thruster capable of operating at 8 W and producing 217 μN of thrust, called the Miniature Microwave Frequency Ion Thruster (MMIT) [25]. Another thruster developed at the same university is the Miniature Radio Frequency Ion Thruster (MRIT), a 1 cm thruster capable of delivering 59 μN of thrust at 13 W of power, with an Isp of 5480 s [26].

However, due to the complexity of downsizing HETs and GITs, nanosatellites have typically used Vacuum Arc Thrusters (VATs) and FEEP thrusters, as they are easier to miniaturise.

One such system, an electrospray thruster measuring 3.8 × 3.8 × 1.5 cm, was developed in the work of Natisin et al. [27]. This thruster, equipped with multiple emitters, demonstrates stable performance from 0.6 mW to 1.3 W with an observed thrust-to-power ratio of 30 μN/W. Another more compact thruster, the NanoFEEP emitter, was developed by TU Dresden [28,29]. With a size fitting in a three cm^3 volume, this emitter provides a thrust of 8 μN for power in the range of 50 to 150 mW.

VATs are an alternative that provides easy miniaturisation, operation at low power, and use of solid propellant. One example of a miniaturised thruster is the μCAT used onboard the BRICSat-P 1.5U CubeSat [30]. Developed by the United States Naval Academy, it is characterised by a specific impulse up to 3000 s and can operate at very low power levels. Another notable example is the Pulsed Plasma Thruster for CubeSat Propulsion (PPTCUP), jointly developed by the University of Southampton and Mars Space Ltd [31,32]. This VAT can operate with power levels as low as 0.3 W and has a miniaturised design, fitting within a 33 mm box. The University of Illinois also developed a miniature VAT with dimensions of 4 × 4 × 4 cm. With an operational power range of 1–100 W and a thrust-to-power ratio of 10 μN/W, this system demonstrates that miniature VATs can still produce thrust levels up to millinewtons [33].

This work introduces HexSats, a concept derived from the DiskSat, for VLEO applications. A thruster concept suitable for flat architecture, the distributed micro-propulsion system, is first introduced in Section 2. Then, Section 3 introduces HexSats by changing the circular profile of

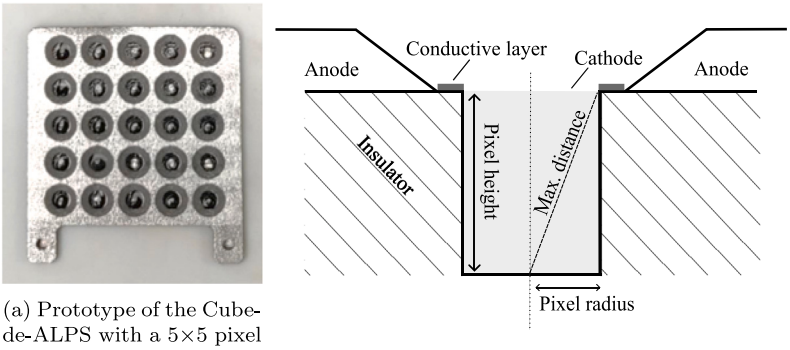

(a) Prototype of the Cube-de-ALPS with a 5×5 pixel grid

(b) Cross-section of a pixel

Fig. 3. Picture of a Cube-de-ALPS prototype and a pixel cross-section.
Source: Images taken and adapted from [37].

DiskSats to a hexagonal shape. Key performance metrics are introduced in Section 4, and their relationship to HexSat size is investigated. Probable operational modes are subsequently detailed in Section 5. Finally, Section 6 analyses the feasibility of HexSats with respect to power in different VLEO operational modes.

2. Distributed micro-propulsion system

The further miniaturisation of the propulsion systems reviewed in Section 1 would allow many thrusters to be placed on a satellite. Therefore we propose a DiskSat design with multiple miniature thrusters distributed along its structure. In this scenario, each thruster head, also called a pixel, would be individually addressable and provide a thrust at the micro-Newton level. While each pixel is fixed on the structure and cannot provide thrust vectoring, positioning them across multiple faces enables complete 3-axis actuation of the spacecraft. It would be possible to not have the pixels on all sides. However, the amount of fuel onboard is proportional to the amount of pixels mounted on the satellite. Therefore, placing pixels on all sides allows for greater fuel reserves and greater flexibility in control of the spacecraft. The satellite can then be precisely controlled by keeping the pixels re-ignitable and the thrust level scalable. We call such a thruster concept a distributed micro (μ)-propulsion system (DμPS). The term "distributed" indicates many thruster heads are spread across the satellite, while "micro-propulsion" refers to both the low thrust level and the small dimensions of the pixels. As shown in Fig. 2, the pixels placed on the thickness of the DiskSat can provide thrust in the $\hat{x}$ and $\hat{y}$ axes, which are parallel to the facesheet. This thrust in the $\hat{x}$ and $\hat{y}$ directions can be used for orbital control. Meanwhile, the pixels arranged on the facesheet can deliver thrust in the $\hat{z}$ direction, which is normal to the facesheet. This thrust in the $\hat{z}$ direction can be used for attitude control.

The DμPS requires a thruster system with a flexible architecture to operate in a distributed configuration, while also presenting small pixels to fit within the thickness of the DiskSats. For this purpose, this work uses the performance parameters of a thin-film VAT analysed by Saddul et al. and prototyped in Saletes et al. as the DμPS [34,35], although the DμPS concept is agnostic towards the specific thrust generation principle. The thin-film VAT is a flat thruster comprising multiple individual pixels of tunable diameter. Each pixel consists of a circular anode surrounding a cathode material, which vaporises upon ignition, effectively acting as fuel. A prototype of this DμPS, including a cross-section of a single pixel, is depicted in Fig. 3. It uses copper as fuel, providing a thrust-to-power ratio of approximately 11.7 μN/W [36].

3. Hexagons are the Bestagons

The previous section has introduced the use of DμPS on a DiskSat. However, the current architecture presents limitations for constellation building, i.e. efficient mass deployment. We introduce the HexSat concept, a thin platform similar to the DiskSat with a hexagonal profile. It uses the DμPS to provide complete orbit and attitude actuation. Transitioning from a circular to a hexagonal profile offers superior packing efficiency inside a rocket fairing, reducing total launch costs. An illustration of the HexSat concept is shown in Fig. 4.

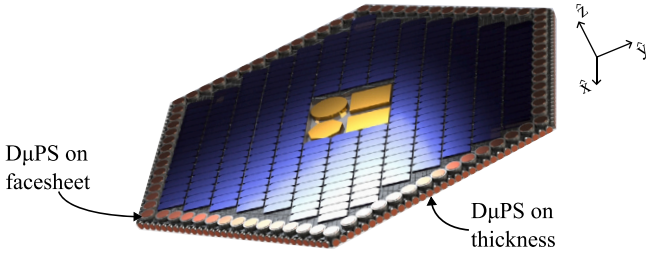

Fig. 4. HexSat concept: A flat hexagonal satellite using the DμPS for orbital and attitude actuation.

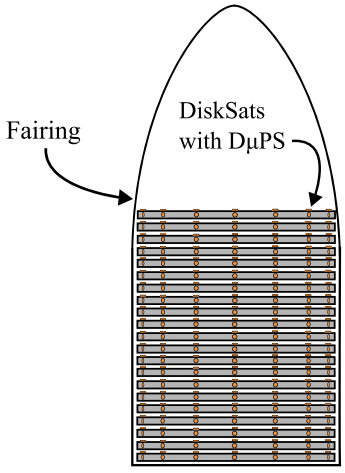

Fig. 5. DiskSats stacked vertically inside a launch vehicle fairing.

We then analyse the orbit and attitude control capabilities of DiskSats, SquareSats and HexSats. Thanks to the non-circular profile, the pixels on the thickness are not all aligned with the centre of mass and can now also control the yaw motion. However, while providing complete 3-axis attitude control, a polygonal profile worsens misalignments between the pixels on the thickness and the thrust direction. For comparison, a SquareSat, using a square profile, is also analysed alongside the DiskSat and HexSat.

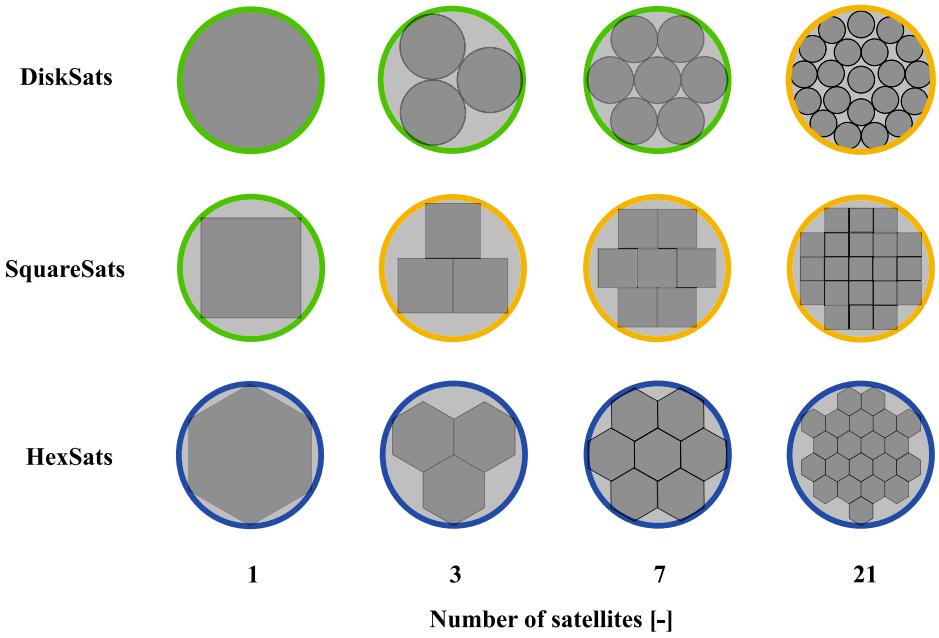

Fig. 6. Packing configurations of DiskSats, SquareSats and HexSats inside a launcher fairing. The configurations proven to be optimal are highlighted in green while the best-known configurations are in orange. Configurations that are conjectured for this work are highlighted in blue. (For interpretation of the references to colour in this figure legend, the reader is referred to the web version of this article.)

Table 1
Control characteristics of DiskSats, SquareSats, and HexSats. The controlled axes, worst-case thrust vector misalignment, and associated required thrust magnitude are illustrated for each satellite architecture. We assumed 100 pixels are mounted on the thickness of the DiskSat for this example.

Shape	Controlled axes	Max. misalignment	Thrust magnitude
DiskSat	$\hat{x}, \hat{y}$	1.8°	1.00049 T_u
SquareSat	$\hat{x}, \hat{y}, \hat{z}$	45°	$\sqrt{2}\, T_u \approx 1.414\, T_u$
HexSat	$\hat{x}, \hat{y}, \hat{z}$	30°	1.1547 T_u

3.1. Packing efficiency

The thin architecture of DiskSats, enabled by DμPS, allows for efficient vertical stacking within rocket fairings, as illustrated in Fig. 5. However, when considering larger rockets, the fairing can accommodate multiple vertical columns of satellites. Unfortunately, the circular shape of the fairings results in inevitable gaps between these columns of satellites, effectively wasting costly space. By minimising the total area of the gaps and thus maximising the packing efficiency, we can ensure a more effective use of the space provided by the launch vehicle.

We present the optimal or best-known layouts for packing discrete numbers of DiskSats, HexSats, and SquareSats inside a given rocket fairing. Where the configuration is proven optimal, it is highlighted in green in Fig. 6, while the best-known solutions found in the literature are highlighted in orange [38–40]. The configurations highlighted in blue represent the best-known solutions for packing hexagonal shapes within a hexagon [38], which we conjecture to be the most efficient configurations for packing HexSats inside a circular fairing.

To quantify the size of satellites allowed by these different configurations, Fig. 7 shows the size of individual satellites for three popular launchers [4]: Falcon 9, Vega and Electron. The sizes of the graphical elements are proportional to their surface area, which are given inside the shapes. If the surface area of the satellite is equal or greater than that of the DiskSat demonstration mission, then the graphical element is highlighted in green. If not, then the shape is highlighted in red.

As expected, the larger the fairing size, the larger the surface area of each satellite. For up to three columns per fairing, the DiskSat geometry provides better packing efficiency and thus a larger satellite than a HexSat. However, for more columns, the HexSat architecture leads to a greater satellite size in a given fairing. The SquareSat profile always performs worse than the corresponding HexSat. Therefore, a HexSat yields the largest surface area when deploying many satellites at once.

3.2. Orbit and attitude control capability

The DiskSat can control its attitude by firing the thrusters on its facesheet, and maintain its orbit by using the thrusters on its thickness. If the pixels on the thickness are not exactly aligned with the desired thrust direction $\vec{u}$, the DiskSat can either first rotate around the $\hat{z}$ axis or ignite two pixels whose thrust vectors will add up to the required thrust direction.

However, the thrust generated by the pixels on the thickness will act through the centre of mass. The DiskSat will therefore not produce any torque around the $\hat{z}$ axis, which is normal to the facesheet, to control the yaw motion. Using a SquareSat or HexSat architecture, the DμPS can control the $\hat{z}$ axis, providing complete 3-axis satellite control. The straight sides, however, mean that thrust can only be produced in four or six different directions for orbital manoeuvres. This means potentially larger misalignment relative to the desired thrust direction compared to the DiskSat architecture. Fig. 8 illustrates each shape firing in a worst-case misalignment. The required thrust magnitude for a pixel T_{req} will then need to be augmented to account for the sub-optimal thrust direction according to

$$T_{req} = \frac{T_u}{\cos(\delta)} \tag{1}$$

where T_u is the required thrust magnitude acting in the desired direction $\vec{u}$, and δ is the angular misalignment.

For a DiskSat, the thrust misalignment is limited to half of the angular separation between each pixel. For example, with 100 pixels on

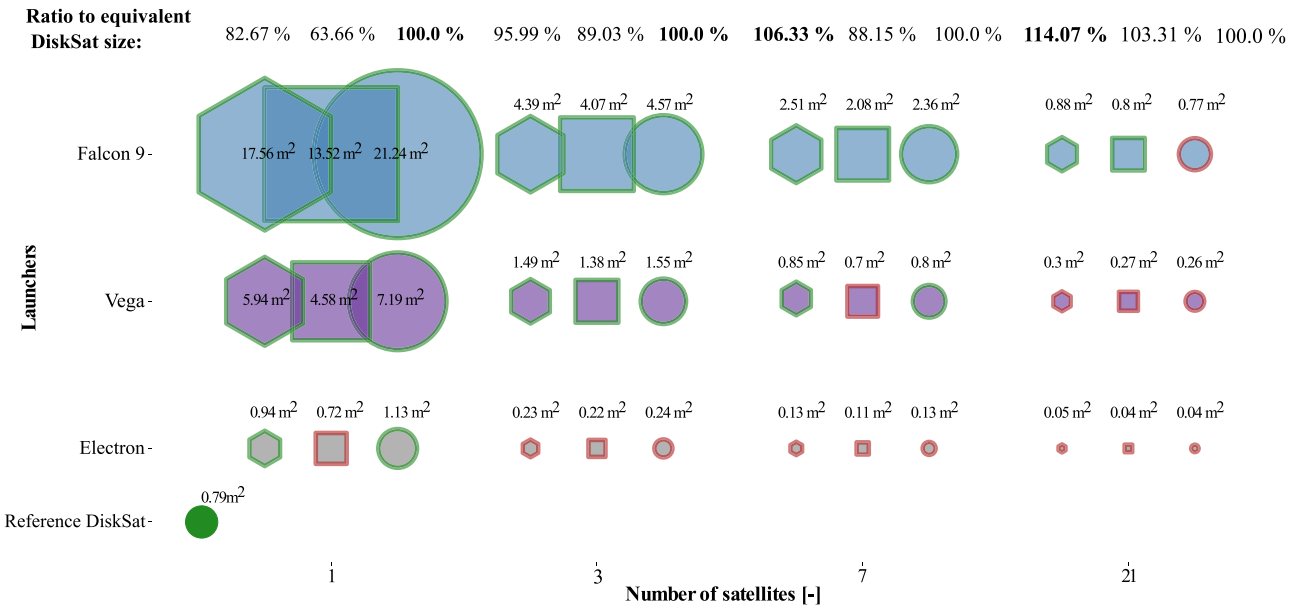

Fig. 7. Individual satellite sizes for different numbers of satellite columns in the Electron, Vega and Falcon 9 launchers. If the surface area of is greater than the DiskSat demonstration mission, then it is highlighted in green. If not then the shape is highlighted in red. (For interpretation of the references to colour in this figure legend, the reader is referred to the web version of this article.)

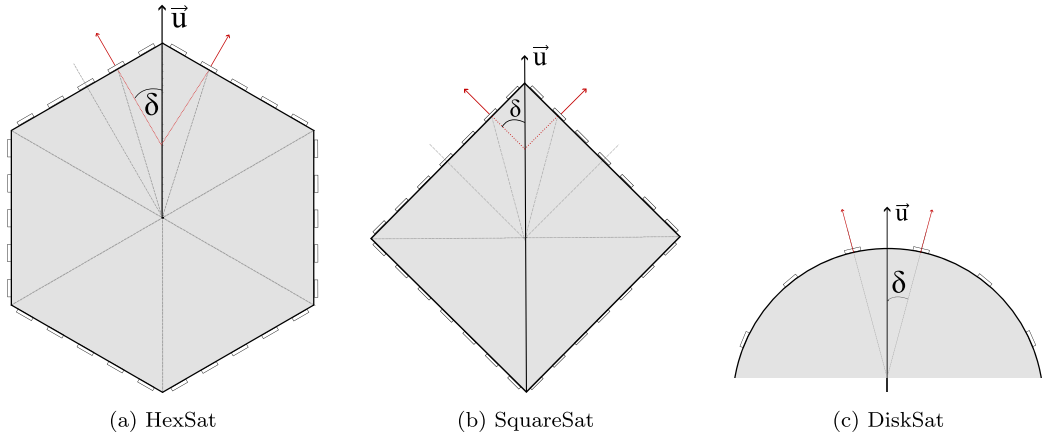

Fig. 8. Maximum thrust misalignments for HexSats, SquareSats and DiskSats.

the thickness, the maximum angular misalignment is $\delta_{max}^{disk} = 1.8°$. For HexSats and SquareSats, the maximum misalignment is half the angle formed by their respective diagonals, which leads to $\delta_{max}^{hex} = 30°$ and $\delta_{max}^{sq} = 45°$ respectively.

Table 1 specifies, for a worst-case misalignment, the required increase in thrust magnitude to deliver the desired acceleration in the direction $\vec{u}$. Using a HexSat allows complete 3-axis control while reducing thrust direction misalignment. Thus, compared to a SquareSat, a HexSat requires less increase in thrust to achieve the target acceleration in the desired direction $\vec{u}$. While the thrust misalignment can be corrected by rotating around the $\hat{z}$ axis, this analysis is important in scenarios where no time is allowed for an attitude manoeuvre (i.e. constant 'real-time' drag compensation) or if the DμPS has burnt out many pixels and is unable to rotate the satellite.

To summarise, for launch configurations with more than three satellite columns HexSats provide the best packing efficiency and naturally allow 3-axis control with limited thrust misalignment. The HexSat geometry is also likely easier to manufacture due to its straight lines compared to the curved geometry of DiskSats.

4. HexSat performance

To better understand the capabilities of the HexSat concept, we investigate three key performance metrics for a HexSat in VLEO as a function of its size. These metrics are

1. the orbit-average power P_{avg}^{gen}
2. the change in angular velocity $\Delta\omega$ ("maneuverability")
3. the peak angular acceleration $\dot{\omega}_{peak}$ ("agility")

We present equations that express the performance metrics as functions of the HexSat's side-length and design parameters. The analysis is based on specific values for the design parameters, which are provided in Table 2. Furthermore, the inertia matrix of a HexSat of assumed uniform density ρ_{Disk} with side-length s and thickness t is given by

$$\mathbf{I}_{hex} = \frac{\sqrt{3}}{8} s^2 t \rho_{Disk} \begin{pmatrix} \frac{5}{2}s^2 + t^2 & & \\ & \frac{5}{2}s^2 + t^2 & \\ & & 5s^2 \end{pmatrix}. \quad (2)$$

Table 2
Summary of DμPS and HexSat properties.

Property	Symbol	Value
Pixel mass [mg]	m_{pixel}	0.912
Pixel radius [mm]	R_{pixel}	4.5
Thrust-to-power ratio [μN/W]	T_p	11.65
Mass flow rate [μg/s]	$\dot{m}_f$	1.4
DiskSat density [kg /m^3]	ρ_{Disk}	407.44
DiskSat thickness [cm]	t	2.5
Solar array efficiency [–]	η_{SA}	15%
Solar flux at earth [W/m^2]	S_{flux}	1400

The density ρ_{Disk} and thickness t have been chosen to match the properties of the DiskSat demonstration missions. The side-length s remains a variable to analyse the scalability of the HexSat performance metrics.

4.1. Orbit-average power

The instantaneous power generated along an orbit will vary based on the angle between the normal to the solar cells and the Sun vector. Assuming the HexSat maintains constant Nadir pointing, the normal to the solar cells can be approximated to the radial unit vector $\hat{r}_{orb}$,

$$P_{gen} = \begin{cases} \sigma P_{peak} \left(\hat{r}_{Sun} \cdot \hat{r}_{orb}\right) & \text{if } \hat{r}_{Sun} \cdot \hat{r}_{orb} \geq 0 \\ 0 & \text{else} \end{cases} \tag{3}$$

where $\hat{r}_{Sun}$ is the direction pointing towards the Sun from the HexSat and the shadow function σ denotes the fraction of the solar disk visible from the HexSat's position, and depends on the orbital parameters [41, 42]. The variable P_{peak} is the maximum power the solar array can generate in ideal conditions, which depends on the area of the HexSat and is given by

$$P_{peak} = \eta_{SA} S_{flux} \frac{3\sqrt{3}}{2} s^2 \tag{4}$$

where the solar flux at the Earth is S_{flux} and the efficiency of the solar panels is η_{SA}. For this work, we used the peak power of the demonstration DiskSats and assumed the solar panels completely covered the facesheet, leading to $\eta_{SA} = 15\%$.

Averaging the generated power over a full orbital period τ_{orbit} yields the average power as

$$P_{avg}^{gen} = \frac{1}{\tau_{orbit}} \int_0^{\tau_{orbit}} P_{gen}\, dt. \tag{5}$$

Depending on the orbital parameters, the HexSat will generate varying amounts of average power over an orbit, as shown on Fig. 9. For this plot, it is assumed the RAAN is measured from the direction of the Sun, as illustrated in Fig. 10.

The results shown in Fig. 11 are generated for a 250 km circular orbit where the Sun vector $\hat{r}_{Sun}$ lies in the orbital plane. We notice the orbit-average power grows with s^2, making a greater HexSat more desirable.

4.2. Manoeuvrability

To analytically estimate the total change in angular velocity that the HexSat can deliver, we first compute the cumulative angular momentum change imparted by each pixel on the HexSat for each rotational axis. Then, we use the satellite's inertia to obtain the corresponding total change in angular velocity.

A given pixel i will produce a thrust $\vec{T}_i$, which depends on the power P used to operate the DμPS. For a constant thrust which is applied for a firing time Δt_i, the change in angular momentum $\Delta\vec{h}_i$ is

$$\Delta\vec{h}_i = \left(\vec{r}_i \times \vec{T}_i\right) \Delta t_i = \vec{r}_i \times \left(T_p P \hat{T}_i\right) \Delta t_i \tag{6}$$

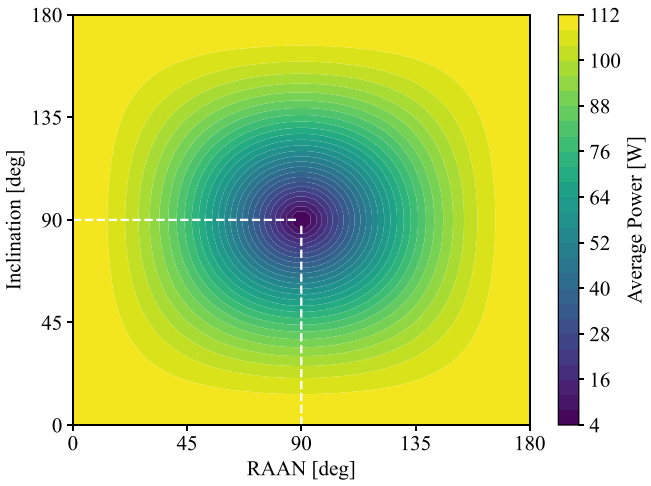

Fig. 9. Orbit-average power as a function of inflation and RAAN, which change the orbit orientation relative to the Sun.

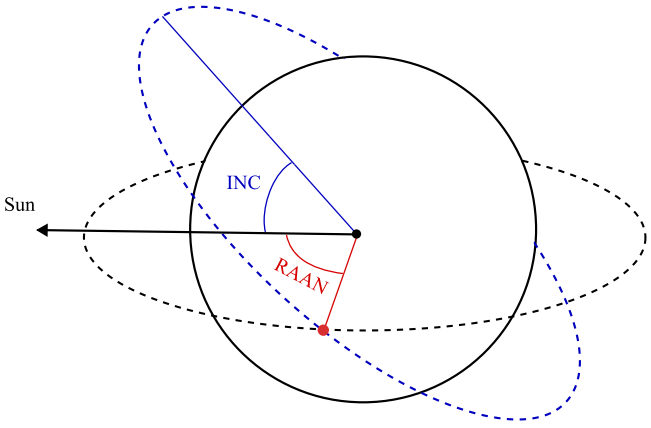

Fig. 10. Measurement of inclination (INC) and RAAN relative to the Sun.

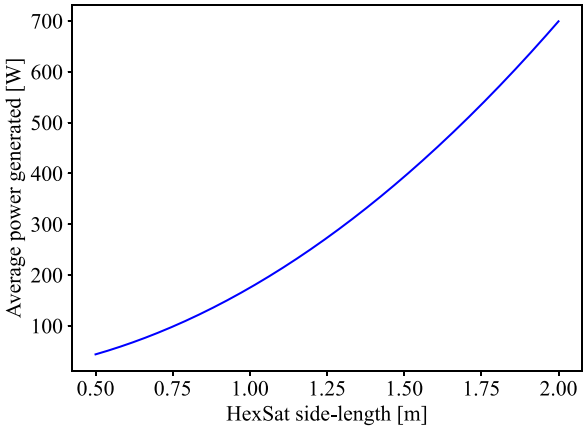

Fig. 11. Orbit-average power of a HexSat as a function of side-length, assuming a circular orbit at 250 km with the Sun vector in the orbital plane.

where $\vec{r}_i$ is the position of the pixel, and T_p is the thrust-to-power ratio. Since the HexSat has many pixels, the total change in angular momentum it can deliver is the sum of the $\Delta\vec{h}_i$ for all pixels. Vectorially, the sum of all $\Delta\vec{h}_i$ is zero because every pixel has a counterpart placed symmetrically opposite, cancelling the net momentum change. However, the pixels will not all fire simultaneously but operate to

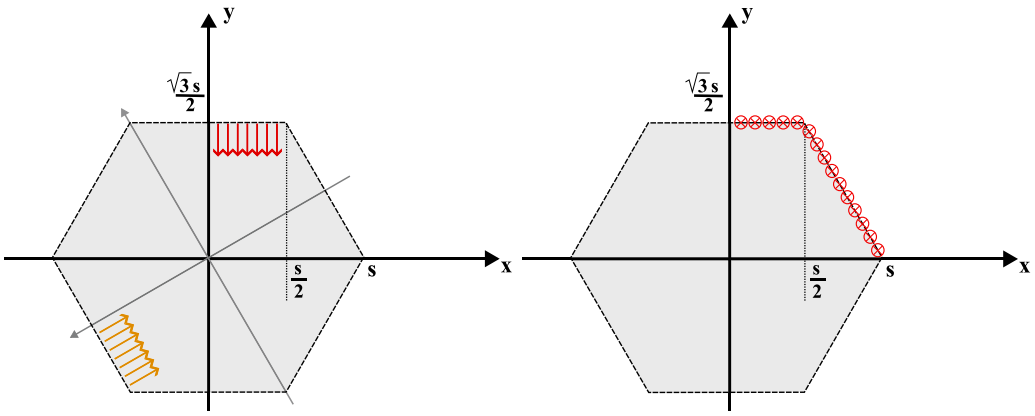

(a) Thruster firing in the $\hat{x}-\hat{y}$ plane (b) Thruster firing parallel to the $\hat{z}$ axis

Fig. 12. Forces generated by the DμPS on a HexSat. The red and orange arrows represent the forces generating torques around the $\hat{z}$ axis, while torques around the $\hat{x}$ and $\hat{y}$ axes will be created by the forces illustrated with ⊗. The analysis is simplified thanks to the symmetry of the HexSat.

provide a desired change in angular velocity. We therefore focus on the magnitude of momentum around each axis,

$$\Delta h_{x,y,z} = \sum_{i=0}^{n_{pixel}} \left| \left(\Delta \vec{h}_i \right)_{x,y,z} \right|. \tag{7}$$

Due to the same symmetrical configuration, the maximum change in angular momentum is limited to half the value given by Eq. (7).

Since the radius R_{pixel} of each pixel is small compared to the side-length of the HexSat, we model the pixels as uniformly distributed along a curve described by the continuous function $\vec{r}(s)$. Instead of considering discrete pixels i with a mass m_{pixel}, we consider infinitesimally small pixels with a mass dm. The pixels have an infinitesimal firing time dt, which depends on the pixel mass $dm = \rho_m \, dl$, the mass flow rate, and the operational power.

As the total fuel mass is uniformly distributed between the pixels, we obtain the mass density ρ_m by dividing the total mass along $\vec{r}(s)$ by its line length L. We approximate the total mass along $\vec{r}(s)$ by multiplying the pixel mass m_{pixel} by the number of pixels n_{pixels}, which can be estimated by dividing L by the diameter of a pixel,

$$dt = \frac{\rho_m}{P\dot{m}_f} \, dl = \frac{m_{pixel} n_{pixel}}{LP\dot{m}_f} \, dl = \frac{m_{pixel}}{LP\dot{m}_f} \left\lfloor \frac{L}{2R_{pixel}} \right\rfloor \, dl \tag{8}$$

where $\dot{m}_f$ is the propellant mass flow rate at 1 W.

Combining Eqs. (6), (7) and (8), we obtain the expression for the angular momentum change deliverable by the HexSat,

$$\Delta h_{x,y,z} = T_p \frac{m_{pixel}}{L\dot{m}_f} \left\lfloor \frac{L}{2R_{pixel}} \right\rfloor \int \left| \left(\vec{r}(s) \times \hat{T} \right)_{x,y,z} \right| \, dl \tag{9}$$

Since we modelled the thrust generation as linearly dependent on P, and the firing time as inversely proportional to P, the angular momentum change is independent of the power.

Total $\Delta\omega_z$

We now specialise Eq. (9) for the pixel in the thickness. Due to the layout of the DμPS on the HexSats, rotation around the $\hat{z}$ axis, which is normal to the facesheet, can only be controlled by pixels in the thickness. Therefore, pixels on the facesheet are excluded when calculating $\Delta\omega_z$.

As shown in Fig. 12(a), all pixels along a single side-length of the HexSat produce thrust in the same direction. Additionally, the side-length exhibits symmetry around its midpoint. The change in angular momentum induced by pixels on one half of a side-length is equal in magnitude but opposite in direction to the contribution from the corresponding other half. This symmetry is present on all six sides of the HexSat, enabling us to restrict our analysis to a single half-side-length. The total change in angular momentum is then twelve times the Δh computed for half the side-length.

By inspecting Fig. 12(a), we observe that the moment arm of a pixel increases linearly between the midpoint of the side-length and its corner. We can therefore simplify Eq. (9) to

$$\Delta h_z = 24 T_p \frac{m_{pixel}}{s\dot{m}_f} \left\lfloor \frac{s}{4R_{pixel}} \right\rfloor \int_0^{\frac{s}{2}} x \, dx. \tag{10}$$

The resulting expression for the total angular momentum change around the $\hat{z}$ axis is

$$\Delta h_z = 3 T_p \frac{m_{pixel}}{\dot{m}_f} \left\lfloor \frac{s}{4R_{pixel}} \right\rfloor s. \tag{11}$$

Eq. (11) shows that Δh_z grows with s^2. However, according to Eq. (2), the inertia of a HexSat grows proportionally to s^4. The total *angular velocity* change $\Delta\omega_z$, computed with $\Delta h_z / I^{zz}_{hex}$, is thus inversely proportional to s^2.

Total $\Delta\omega_{x,y}$

A similar approach is used to specialise Eq. (9) for the pixels on the facesheet. Pixels on the thickness can be ignored, as they do not provide a torque around the $\hat{x}$ or $\hat{y}$ axes.

Some pixels on the facesheet will generate momentum around both the $\hat{x}$ and $\hat{y}$ axes, as shown in Fig. 12(b). This can be accounted for by summing the momentum components,

$$\Delta h_{x,y} = \sqrt{\Delta h_x^2 + \Delta h_y^2}. \tag{12}$$

We note from Fig. 12(b) that the HexSat presents a mirror symmetry along the $\hat{x}$ and $\hat{y}$ axes, allowing us to restrict our analysis to a quarter of the satellite, as depicted. Again, the function for the moment arm is the curve delimiting the shape of the HexSat. Therefore, Eq. (9) becomes

$$\Delta h_x = \Delta h_y = 8 T_p \frac{m_{pixel}}{3s\dot{m}_f} \left\lfloor \frac{3s}{4R_{pixel}} \right\rfloor \times \left(\int_0^{\frac{s}{2}} \frac{\sqrt{3}}{2} s \, dx + \int_{\frac{s}{2}}^{s} -\sqrt{3}x + \sqrt{3}s \, dx \right). \tag{13}$$

The final expression for the total Δh around the $\hat{x}$ and $\hat{y}$ axes is

$$\Delta h_{\hat{x},\hat{y}} = \sqrt{6} T_p \frac{m_{pixel}}{\dot{m}_f} \left\lfloor \frac{3s}{4R_{pixel}} \right\rfloor s. \tag{14}$$

Eq. (14) shows that the Δh around $\hat{x}$ and $\hat{y}$ increases with s^2, similarly to the Δh around $\hat{z}$. Again, because the inertia grows with s^4, this means the total deliverable change in *angular velocity* around each axis actually decreases with s^2, as shown in Fig. 13.

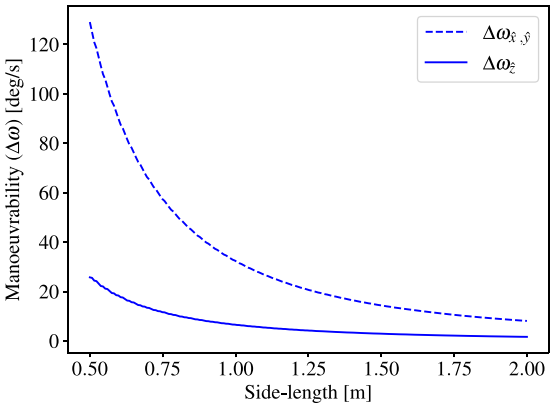

Fig. 13. Deliverable angular velocity around the $\hat{x}$, $\hat{y}$ and $\hat{z}$ axes.

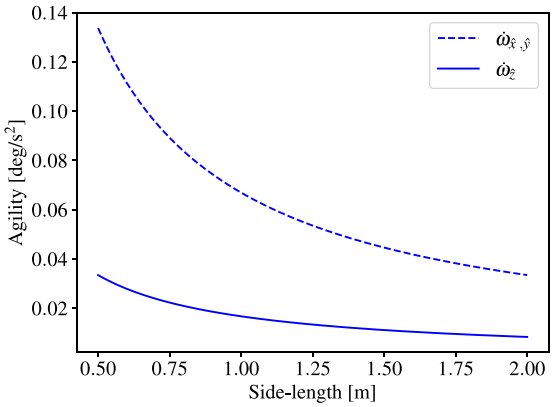

Fig. 14. HexSat agility as a function of its side-length for the $\hat{x}$, $\hat{y}$ and $\hat{z}$ axes.

4.3. Agility

To compute the agility $\dot{\omega}_{peak}$, we fire a single pixel, located on the corner of a HexSat, using the maximum power P_{peak} available to the HexSat. This produces a peak torque $\vec{\tau}_{peak}$, which can then be transformed into a peak acceleration thanks to the inertia of the satellite. The maximum power directly influences the peak torque $\vec{\tau}_{peak}$ that the DμPS can generate, which can be expressed as

$$\vec{\tau}_{peak} = \vec{r}_{corner} \times T_p P_{peak} \hat{T} \tag{15}$$

where $\vec{r}_{corner}$ is the position a pixel at a corner. The peak power P_{peak} is determined with Eq. (4). Due to the layout of the DμPS on the HexSat, only the pixels on the thickness will produce a torque around the $\hat{z}$ axis. As depicted in Fig. 12(a), the moment arm around the $\hat{z}$ axis of a pixel in the corner is half a side-length. The choice of corner will change the direction of the torque, but not its magnitude. Therefore, the magnitude of the peak torque around the $\hat{z}$ axis is

$$\tau_{peak,z} = \frac{3\sqrt{3}}{4} \eta_{SA} S_{flux} T_p s^3 \tag{16}$$

where the peak power P_{peak} is replaced with Eq. (4).

We compute the peak torque from the pixels on the facesheet with a similar approach. Again, the choice of corner will change the direction of the peak torque, but not its magnitude. We thus select the pixel located on the $\hat{x}$ axis at a distance s from the centre of mass, as shown in Fig. 12(b). The magnitude of the peak torque around the $\hat{x}$ and $\hat{y}$ axes is

$$\tau_{peak,xy} = \frac{3\sqrt{3}}{2} \eta_{SA} S_{flux} T_p s^3. \tag{17}$$

Both the peak torques around the $\hat{x} - \hat{y}$ and $\hat{z}$ directions are proportional to s^3. However, the satellite's inertia grows with s^4, as shown in Eq. (2). Therefore, the agility, computed with τ_{peak}/I_{hex}, is inversely proportional to s, as shown in Fig. 14.

In summary, while a greater HexSat size is desirable to generate more power, the increased inertia of the satellite will lead to reduced agility ($\dot{\omega}_{peak}$) and less total manoeuvrability ($\Delta\omega$). Because the minimum agility required depends on the specific mission profile, we explore the HexSat operational modes in Section 5.

5. Operational mode & orbit geometries

The VLEO regime's advantages mainly apply to missions focusing on the Earth, such as remote sensing or communication constellations. Satellites are therefore likely to keep a Nadir-pointing orientation or briefly track a target on the ground. This section details the requirements for constant Nadir pointing and Active Ground Tracking operational modes. Depending on the mode of operation, the satellite's projected frontal area will vary, changing the experienced drag. Expressions to compute the drag forces are provided, and the minimum acceleration profiles required to execute each operational mode are presented.

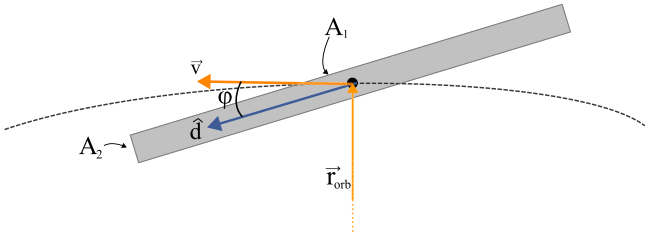

Fig. 15. Geometry of the drag forces affecting a HexSat in VLEO.

5.1. Drag compensation

No matter the operational mode, due to the high atmospheric density of VLEO, most satellites will have to use their thrusters to prevent premature de-orbiting. The onboard propulsion can maintain the spacecraft's orbit by applying an equal and opposite force to the drag experienced. In this scenario, the thin form factor of the HexSats allows for a small frontal area to be produced, which yields a smaller drag and thus reduces the load on the propulsion system. However, this advantage only applies if a HexSat is flying in its minimal drag configuration. If the minimum drag direction, represented by $\hat{d}$ in Fig. 15, is not aligned with the velocity vector $\vec{v}$, then the spacecraft will experience a greater drag. In this section, we analyse the minimum drag the DμPS must compensate based on the spacecraft's attitude.

The drag experienced by a spacecraft can be modelled using

$$D = \frac{1}{2} \rho_{atm}\left(\vec{r}_{orb}\right) v^2 \left(A_1 C_{D,1}(\varphi) + A_2 C_{D,2}(\varphi)\right) \tag{18}$$

where ρ_{atm} is the atmospheric density, a function of orbital position $\vec{r}_{orb}$, $\vec{v}$ is the spacecraft's orbital velocity, and C_D is the drag coefficient and is a function of φ, the angle between the velocity vector and $\hat{d}$. The variable φ is called the angle of attack and is a function of time t. In this work, the drag coefficient C_D is computed using a free molecule theory model derived by Sentman, in the form presented by Sutton [43,44]. The HexSat is represented using two thin plates: one for the facesheet denoted as A_1, and one for the thickness denoted as A_2. Their C_D are different as they have different dependencies on φ, i.e. the drag induced by the thickness is maximum when the facesheet is parallel to $\vec{v}$ and produces no drag.

The atmospheric density is modelled through an interpolation of the Jacchia-77 atmospheric model introduced in Frey and Colombo [45],

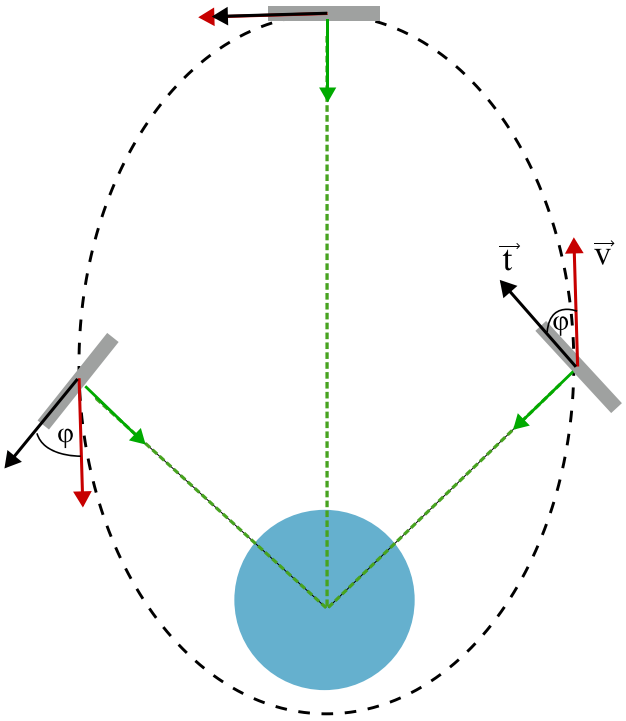

Fig. 16. Constant Nadir-pointing mode: the spacecraft's instruments are always aligned towards the centre of the Earth.

which allows for both static and temperature-dependent models. However, these choices do not restrict the following analysis and can be replaced by different models if desired.

In Eq. (18), the variables $\vec{r}_{orb}$, $\vec{v}$, ρ_{atm} and the HexSat area can be determined from the chosen orbit and satellite geometry. However, computing the projected area and the drag coefficient requires knowledge of φ, which depends on the operational mode. The following subsections describe how a given operational mode can be maintained and its subsequent effect on the angle of attack profile.

5.2. Nadir pointing

Maintaining a Nadir position allows the spacecraft to keep its instruments pointed directly at the Earth at all times. For this work, we use the geocentric Nadir direction which points directly towards the centre of the Earth from the spacecraft [46]. Therefore, the satellite must rotate at the same angular speed as the position vector to keep its instruments aligned with the Nadir direction. The DμPS must provide this precise acceleration profile to operate in this mode, unless the orbit is circular, in which case no angular acceleration is needed.

We can compute the angular velocity required for constant Nadir pointing in a given orbit with [47]

$$\dot{\theta} = \frac{na^2}{r_{orb}^2}\sqrt{1-e^2} \tag{19}$$

where n is the mean orbital motion, a is the semi-major axis, and e is the eccentricity. The function r_{orb} is the orbital radius, which depends on the true anomaly θ

$$r_{orb} = \frac{a\left(1-e^2\right)}{1+e\cos(\theta)}. \tag{20}$$

We then can obtain the angular acceleration by taking the time derivative

$$\ddot{\theta} = \frac{d\dot{\theta}}{dt} = \frac{d\dot{\theta}}{d\theta}\frac{d\theta}{dt} = \frac{d\dot{\theta}}{d\theta}\dot{\theta} \tag{21}$$

which leads to the final expression of the angular acceleration

$$\ddot{\theta} = -\frac{2n^2 e\sin(\theta)\left(1+e\cos(\theta)\right)^3}{\left(1-e^2\right)^3}. \tag{22}$$

The HexSat must be capable of providing the full range of angular accelerations determined by Eq. (22) to correctly track the Nadir direction. If the HexSat follows this angular acceleration profile, its angle of attack profile can also be computed. Because the HexSat must have its instruments aligned with the position vector in Nadir pointing, the vector $\hat{d}$ is always perpendicular to the position vector, as shown in Fig. 16. Therefore, the angle of attack φ becomes the angle between the velocity vector $\vec{v}$ and the normal to the position vector, or the flight path angle [47]. It is given by

$$\varphi = \arctan\left(\frac{e\sin\theta}{1+e\cos\theta}\right). \tag{23}$$

Fig. 17(a) shows the acceleration profiles required to maintain Nadir pointing for orbits with a fixed perigee at 250 km. The corresponding angles of attack along the orbit are shown in Fig. 17(b). Note that the angular acceleration required to maintain Nadir pointing in a circular orbit is zero as no variation in the angular velocity is needed. Similarly, for the non-circular orbits, the angle of attack remains small due to the low eccentricity.

5.3. Active ground tracking

Active Ground Tracking (AGT) refers to the HexSat keeping the sensors pointed at a specific point on the ground, called the target, during a fly-over. It is achievable either by rotating the onboard sensors or by turning the spacecraft itself at a precise rate to keep the ground target aligned with the onboard instruments. We assume the HexSat is in a circular orbit and that the target lies on its ground track, specifically at $\theta = 0$.

Unlike the continuous operation of the Nadir pointing mode, AGT requires a duty-cycled approach. The HexSat will track its target throughout the tracking window and then reorient itself to coast in the minimum drag configuration until the next target is acquired.

As shown in Fig. 18, a preparation phase, where the HexSat aligns itself with the target, is required to ensure correct tracking. Similarly, a streamlining manoeuvre, mirroring the preparation, is required to return the HexSat to the minimal drag configuration. The execution of the preparation and streamlining phases ultimately depends on the nature of the HexSat's mission and is therefore not specified. However, the angle between the Nadir direction and the target direction is the same at the end of the preparation phase and at the start of the streamlining phase. This angle is equal to half of the total angular change imparted during the tracking phase. We thus assume the preparation and streamlining phases will each require half the energy consumed during tracking.

To estimate the total AGT cycle time Δt_{AGT}, we further assume that both phases each take half the time of the tracking stage, such that

$$\Delta t_{AGT} = 2\Delta t_{tracking}. \tag{24}$$

Then, the number of AGT cycles n_{cycles} performed during one orbit can be determined with Δt_{AGT} and the duty cycle ζ, the portion of the orbit dedicated to executing the AGT cycle which includes both preparation and streamlining phases,

$$n_{cycles} = \left\lfloor \frac{\tau_{orbit}\zeta}{2\Delta t_{tracking}} \right\rfloor \tag{25}$$

where the variable τ_{orbit} is the orbital period.

During the tracking stage, the HexSat (or its instruments) must be aligned with and rotate at the same angular speed as the relative position vector $\vec{\kappa}$ to actively follow a target on the surface. We are interested in the angular acceleration $\ddot{\alpha}$ required to track the target. Given the geometry shown in Fig. 19, we can express α, the relative

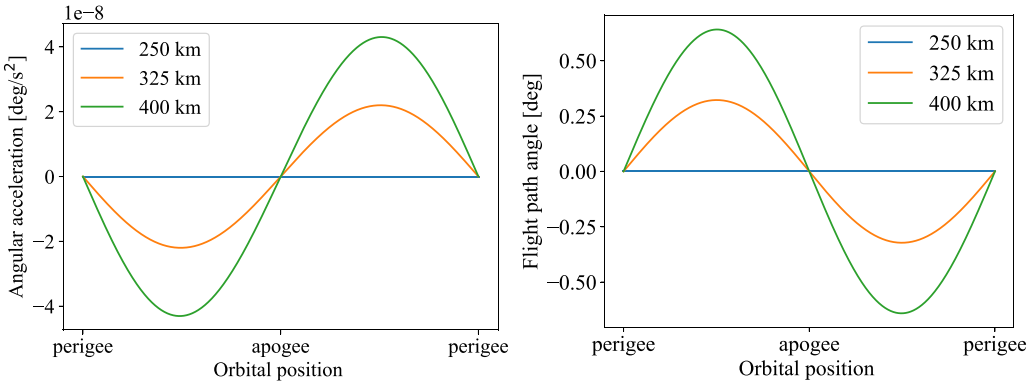

(a) Acceleration profiles (b) Angle of attack

Fig. 17. Required acceleration profile and flight path angle to perform Nadir pointing in low-eccentricity orbits with varying apogees. The perigee is fixed at 250 km for all orbits.

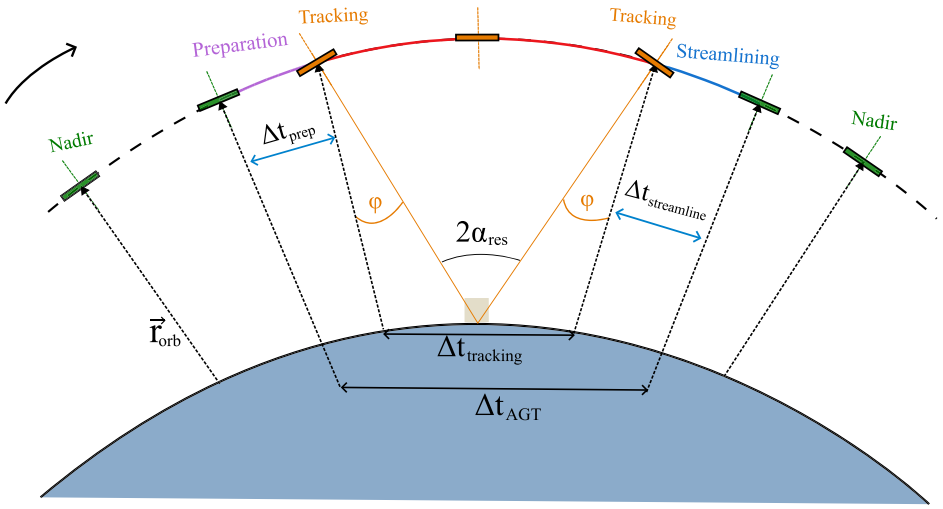

Fig. 18. Sketch of a full Active Ground Tracking cycle, including preparation, tracking, and streamlining.

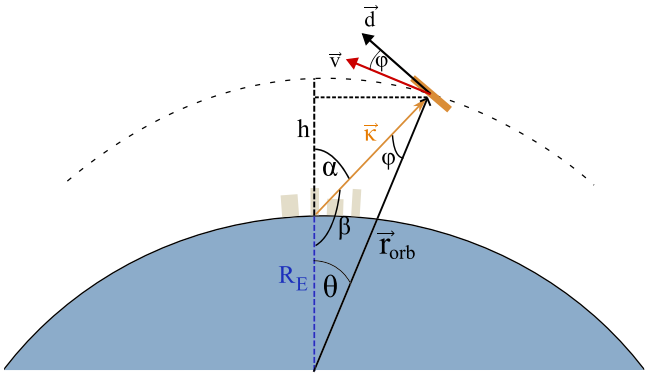

Fig. 19. Active ground tracking mode: the spacecraft's instrument briefly point at a target on its ground track.

angular position, as a function of the true anomaly θ through the sine projection of $\vec{r}_{orb}$,

$$\alpha = \arcsin\left(\frac{r_{orb}}{\kappa}\sin(\theta)\right) \tag{26}$$

where κ is the distance between the target and the satellite, called the slant range and θ is the true anomaly, measured from the target. The variables κ and r_{orb} are both dependent on the true anomaly θ but are written concisely for readability.

We obtain κ by applying the cosine law

$$\kappa = \sqrt{R_E^2 + r_{orb}^2 - 2r_{orb}R_E\cos(\theta)} \tag{27}$$

where R_E is the radius of the Earth. For a nominal circular orbit of 250 km, the magnitude of κ is greater than 350 km at values of $\theta \geq 2°$. At this distance, the satellite instruments are unlikely to provide a significant advantage compared to using instruments onboard the satellites at higher altitudes. Therefore, in this analysis AGT is limited to a useful tracking window θ_{res} spanning about 2 degrees on each side of the target, as measured at the Earth's centre. It provides approximately one minute of tracking time, leading the total cycle to last around two minutes.

Taking the time derivative, we obtain the angular velocity,

$$\dot{\alpha} = \frac{d\alpha}{d\theta}\dot{\theta}. \tag{28}$$

Similarly, we compute the angular acceleration with the chain rule,

$$\ddot{\alpha} = \frac{d^2\alpha}{d\theta^2}(\dot{\theta})^2 + \frac{d\alpha}{d\theta}\ddot{\theta}. \tag{29}$$

Again, the HexSat must be capable of providing the full range of angular accelerations determined by Eq. (29) to correctly track the ground target. Fig. 20(a) shows an example acceleration profile. In this scenario, we assumed a circular orbit at 250 km and used divided differences to compute the derivatives $\frac{d\alpha}{d\theta}$ and $\frac{d^2\alpha}{d\theta^2}$. As we only considered circular orbits, the vector $\vec{r}_{orb}$ and $\vec{v}$ are orthogonal, which leads the angle between $\vec{\kappa}$ and $\vec{r}_{orb}$ to be the same as the angle of attack φ. We

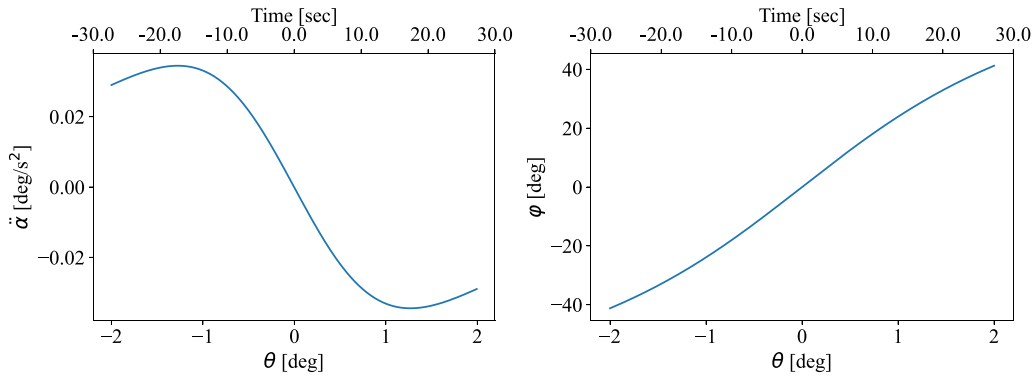

(a) Acceleration profile (b) Angle of attack

Fig. 20. Angular acceleration profile and flight path angle to perform AGT in a 250 km circular orbit over a tracking window of two degrees of true anomaly.

thus compute the angle of attack as

$$\varphi = \alpha - \theta. \tag{30}$$

The angle of attack profile is shown in Fig. 20(b) for a circular orbit at 250 km.

Compared to the Nadir pointing mode, the HexSat in AGT mode will deviate significantly more from the velocity direction. At its peak, the drag force experienced will be up to an order of magnitude higher than in Nadir mode.

6. HexSat power analysis

We investigate the impact of HexSat size on its ability to achieve the operational modes detailed in Section 5. Specifically, we are interested in HexSats that generate more power than they consume. We use the average excess power P_{avg}^{excess} as a measure, defined as

$$P_{avg}^{excess} = P_{avg}^{gen} - P_{avg}^{orbit} \tag{31}$$

where P_{avg}^{orbit} is the average power consumption over one orbit. The average power consumption over one orbital period τ_{orbit} consists of the drag compensation and the attitude manoeuvres,

$$P_{avg}^{orbit} = \frac{E_{orbit}^{drag} + E_{orbit}^{op}}{\tau_{orbit}}, \tag{32}$$

where E_{orbit}^{drag} and E_{orbit}^{op} are the energy consumption due to drag compensation and operational mode respectively. The energy expenditure for drag compensation is calculated by integrating the instantaneous power required to generate a thrust that precisely counteracts the drag force at all times. The energy depends directly on the drag profile D experienced by the HexSat and thus, on the angle of attack profile,

$$E_{orbit}^{drag} = \frac{1}{T_p} \int_0^{\tau_{orbit}} D(\varphi)\, dt. \tag{33}$$

Similarly, the energy required for operational manoeuvres depends on the HexSat inertia matrix $\mathbf{I}_{hex}$ and the required angular acceleration profile $\dot{\omega}$. However, the rotation only acts around either the $\hat{x}$ or $\hat{y}$ axis. Depending on the pixel fired, the DμPS will need to adjust its power level to produce the correct torque,

$$T_p Pr(s) = I_{xx}^{hex} \dot{\omega}. \tag{34}$$

To minimise the operating power level, we fire the pixel with the greatest moment arm, which is located in the HexSat corner at a distance s from the centre of mass. We can then write the energy required as

$$E_{orbit}^{op} = \frac{I_{xx}^{hex}}{T_p s} \int_0^{\tau_{orbit}} \dot{\omega}\, dt. \tag{35}$$

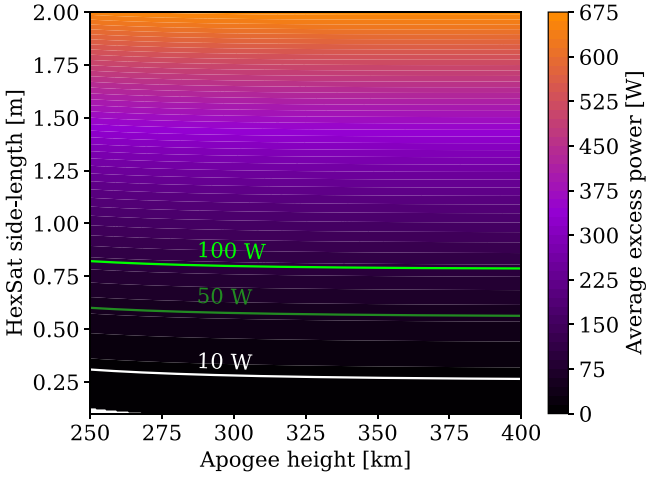

Fig. 21. Excess power based on HexSat size and apogee height, with contour lines indicating 100 W, 50 W and 10 W levels. The perigee is fixed at 250 km.

6.1. Nadir pointing

The energy required to compensate for the drag in constant Nadir pointing mode is computed with Eqs. (18), (23) and (33). Similarly, Eqs. (22) and (35) are used to determine the energy required to maintain the Nadir pointing attitude profile. As shown in Fig. 17(a), the angular accelerations needed for Nadir pointing are minimal, resulting in an average power requirement in the order of 10^{-5} W. It is drag compensation that dominates the DμPS power consumption in this pointing mode. Fig. 21 presents the average excess power available to a HexSat of varying size as a function of apogee altitude, with a perigee fixed at 250 km. The results indicate that while a higher apogee offers a slight increase in available power, the improvement is negligible. Compared to a circular orbit at 250 km, which uses 12 W of average power for drag compensation, an orbit with its apogee at 400 km will use an average of 8 W, assuming a HexSat of equivalent surface area to the demonstration DiskSats. The power required for the thrusters is not significantly reduced as the HexSat will have an increased speed at the perigee. The power saving is also negligible compared to the power generated, which is above 100 W. Therefore, low eccentricity orbits have a negligible impact on the power available to the payload. However, increasing the size of the HexSat significantly increases the excess power. Even in a circular orbit at 250 km, a HexSat with a side-length greater than 0.8 m can generate over 100 W of average excess power, making constant Nadir pointing a viable operational mode.

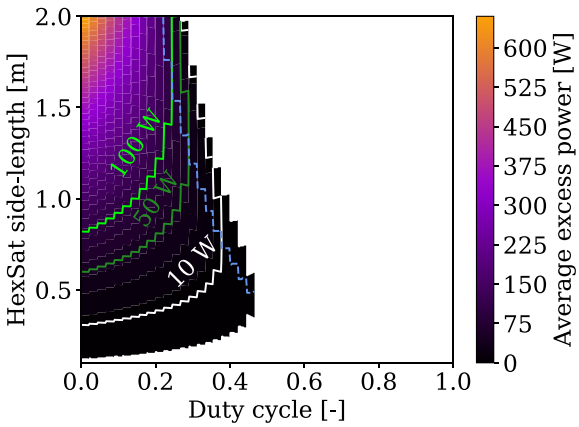

Fig. 22. Excess power based on HexSat size and duty cycle ζ for a 250 km circular orbit. The blue line represents the optimal HexSat size for maximum power at a given duty cycle. (For interpretation of the references to colour in this figure legend, the reader is referred to the web version of this article.)

6.2. AGT

Because an AGT cycle occurs n_{cycles} times across an orbit, we restrict our analysis to a single flyover. As detailed in Section 5, both the preparation and streamlining manoeuvres need half the angular change required for the tracking stage. Consequently, the total energy required to perform the AGT cycle can be expressed as

$$E_{AGT} = E_{prep} + E_{tracking} + E_{streamline} = 2E_{tracking} \tag{36}$$

where $E_{tracking}$ is the energy required to follow a ground-based target actively, i.e. to follow the angular acceleration profile presented in Fig. 20(a). It is now possible to re-write the average power consumed as

$$P_{avg}^{orbit} = \frac{E_{orbit}^{drag} + 2E_{tracking} n_{cycles}}{\tau_{orbit}} \tag{37}$$

where E_{orbit}^{drag} can be computed with Eqs. (18), (30) and (33), while $E_{tracking}$ is determined with Eqs. (29) and

$$E_{tracking} = \frac{I_{xx}^{hex}}{T_p s} \int_0^{\Delta t_{tracking}} \ddot{\alpha}(t)\, dt. \tag{38}$$

While similar to Eq. (35), Eq. (38) integrates only over the tracking time $\Delta t_{tracking}$, as no torques are needed to follow Nadir pointing in circular orbit.

Fig. 22 presents, for a circular orbit at 250 km, the excess power for a HexSat of varying size as a function of the duty cycle ζ. For simplicity, we have kept the power generation model as detailed in Eq. (5), which assumes the spacecraft is constantly in Nadir. While the HexSat's operational mode differs, it effectively spends a maximum of two minutes per target slewing before returning to a Nadir position. At most, the HexSat is 40° offset from the Nadir direction, which corresponds to a 24% decrease in power generation. We therefore believe this assumption to be reasonable as long as the ratio of total AGT cycle time to orbit period, i.e. ζ, remains relatively low.

The results show that if no AGT is performed ($\zeta = 0$), a larger HexSat leads to greater available payload power. However, while the HexSat performs any amount of tracking ($\zeta > 0$), there is an optimal HexSat size that maximises the excess power. This optimal size is marked by the dashed blue line in Fig. 22 for each corresponding duty cycle. The optimum size decreases with increasing duty-cycle as the power consumption includes both the drag compensation and the rotation of the HexSat, which scales with s^3. For a HexSat with the equivalent surface area as the demonstration DiskSat, and a duty cycle of 0.3, the HexSat will use 36 W for tracking and 68 W for drag compensation. However, the power for drag compensation is not always greater than the rotation. As the HexSat grows in size, the power required for rotation will increase with s^3 compared to the power for drag compensation, which increases with s^2. Thus, for a larger HexSat with $s = 1$ with a duty-cycle of 0.3, 216 W will be used for the tracking, while 208 W will be used for drag compensation.

The feasibility of the AGT is dependent on the HexSat side-length s. Small HexSats typically can perform tracking but have low excess power. Larger HexSats can provide high excess power while performing the AGT, although certain combinations of size, altitude and duty cycle are unfeasible. These unfeasible combinations are shown by the white region, where the HexSat is too large and cannot generate enough power to sustain its operation. The step-like profile of the contour plot originates from Eq. (25), where only integer values of n_{cycles} were considered.

The results presented are for circular orbits at 250 km in Fig. 22, and 300 km and 350 km in Fig. 23. We observe that at higher altitudes, more combinations of s and ζ are feasible as the drag is lower, and the overall angular acceleration required is reduced. However, to maximise the advantages of VLEO, we are primarily interested in orbits closer to the Earth. Focusing on the 250 km orbit, a HexSat with a 0.8 m side-length will provide more than 100 W of excess power for a relatively low duty cycle, approximately below 0.2. This translates to approximately 17 min of AGT time, or eight targets tracked across one orbit. Therefore, HexSats are capable of operating in AGT mode at 250 km.

7. Conclusion

The HexSats, a novel concept of flat satellites using a distributed micro (μ)-propulsion system for Very Low Earth Orbits introduced in this work, have significant advantages over traditional CubeSats regarding functional surface area and power generation. The hexagonal design enables complete 3-axis control and increases the usable surface area when multiple vertical stacks of HexSats fit within a launch vehicle fairing. Our investigation of the relationship between DμPS design parameters and the HexSats performance shows that while the orbit-average power increases with size, other performance parameters, such as agility, are inversely proportional to the HexSat size. The results demonstrate that HexSats can operate effectively in Nadir pointing mode in VLEO, although the feasibility of Active Ground Tracking is size-dependent. In a circular orbit at 250 km, a HexSat with a side-length of 0.8 m in Active Ground Tracking can track up to 8 targets per orbit while still delivering more than 100 W of average excess power to the payload.

CRediT authorship contribution statement

Kash Saddul: Writing – review & editing, Writing – original draft, Methodology, Investigation, Formal analysis, Conceptualization. **James Saletes:** Writing – review & editing, Conceptualization. **Minkwan Kim:** Writing – review & editing, Funding acquisition, Conceptualization. **Alexander Wittig:** Writing – review & editing, Validation, Supervision, Methodology, Conceptualization.

Declaration of competing interest

The authors declare that they have no known competing financial interests or personal relationships that could have appeared to influence the work reported in this paper.

Acknowledgements

The authors acknowledge the use of the IRIDIS High-Performance Computing Facility and associated support services at the University of Southampton, in the completion of this work.

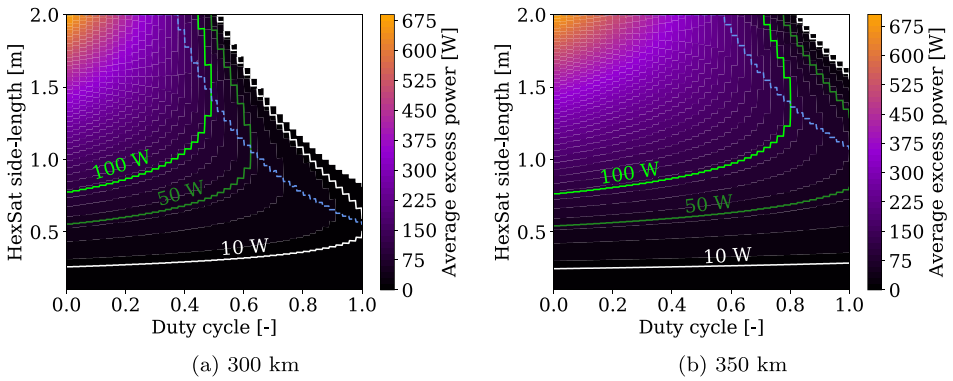

Fig. 23. Excess power based on HexSat size, duty cycle ζ and orbit height. The blue line represents the optimal HexSat size for maximum power at a given duty cycle. (For interpretation of the references to colour in this figure legend, the reader is referred to the web version of this article.)

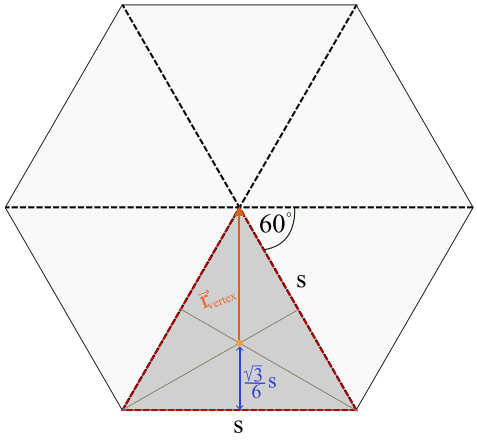

Fig. A.24. Six equilateral triangles can be used to form a regular hexagon.

Appendix. Inertia matrix for a hexagonal plate

We derive the inertia matrix for a hexagonal plate of side-length s and thickness t, assuming a homogeneous and constant density ρ. A regular hexagon is composed of six equal equilateral triangles successively rotated by 60°, as shown on Fig. A.24.

We derive the inertia matrix of an equilateral triangle of side-length s around its centre of mass using the definition of the inertia matrix

$$\mathbf{I} = \int_V \rho \left(r^2 \mathbf{E} - \vec{r}\vec{r}^T \right) \, dV \tag{A.1}$$

where $\mathbf{E}$ is the identity matrix and $\vec{r}$ is the vector from the centre of the reference frame to the element dV. The inertia matrix becomes

$$I_{tri}^{CoM} = \begin{pmatrix} \frac{m}{24}\left(s^2 + 2t^2\right) & & \\ & \frac{m}{24}\left(s^2 + 2t^2\right) & \\ & & \frac{m}{12}s^2 \end{pmatrix}. \tag{A.2}$$

We then shift the inertia tensor of the equilateral triangle to its vertex by using the parallel axis theorem [48],

$$\mathbf{I}_{tri}^{vertex} = \mathbf{I}_{tri}^{CoM} + m_{tri}\left(r_{vertex}^2 \mathbf{E} - \vec{r}_{vertex}\vec{r}_{vertex}^T \right) \tag{A.3}$$

where $\mathbf{I}_{vertex}$ represents the shifted inertia matrix, and $\vec{r}_{vertex}$ is the vector from the centre of mass to the edge of the triangle. The variable m_{tri} represents the mass of the triangle. Assuming a constant and homogeneous density ρ, the mass is given by

$$m_{tri} = \rho A_{tri} t = \rho \frac{\sqrt{3}}{4} s^2 t. \tag{A.4}$$

We then can rotate this inertia matrix with

$$\mathbf{I}_{tri}^{rot} = \mathbf{R}\mathbf{I}_{tri}^{shift}\mathbf{R}^T \tag{A.5}$$

where $\mathbf{R}$ is a rotation matrix describing a pure $\hat{z}$ axis rotation [47],

$$\mathbf{R} = \begin{pmatrix} \cos\phi_i & \sin\phi_i & 0 \\ -\sin\phi_i & \cos\phi_i & 0 \\ 0 & 0 & 1 \end{pmatrix}, \tag{A.6}$$

with

$$\phi_i \in \left\{ 0°, 60°, 12°, 180°, 240°, 300° \right\}. \tag{A.7}$$

Analytically combining the above expressions, we obtain the final inertia matrix of a hexagonal plate of uniform density around its centre of mass as

$$\mathbf{I}_{hex}^{CoM} = \frac{\sqrt{3}}{8} s^2 t \rho_{Disk} \begin{pmatrix} \frac{5}{2}s^2 + t^2 & & \\ & \frac{5}{2}s^2 + t^2 & \\ & & 5s^2 \end{pmatrix}. \tag{A.8}$$

References

[1] K. Woellert, P. Ehrenfreund, A.J. Ricco, H. Hertzfeld, Cubesats: Cost-effective science and technology platforms for emerging and developing nations, Adv. Space Res. 47 (4) (2011) 663–684, http://dx.doi.org/10.1016/j.asr.2010.10.009.

[2] S. Lee, A. Hutputanasin, A. Toorian, W. Lan, R. Munakata, J. Carnahan, D. Pignatelli, A. Mehrparvar, Cubesat design specification rev. 13, CubeSat Program, Calif. Polytech. State 8651 (2009) 22.

[3] NASA, State - of - the - Art Small Spacecraft Technology, 2021, (October) NASA/TP–2020–5008734.

[4] E. Kulu, Nanosat Database, URL https://www.nanosats.eu/.

[5] N.M. Suhadis, Statistical overview of cubesat mission, Lect. Notes Mech. Eng., Vol. March 2003, Springer Singapore, 2020, pp. 563–573, http://dx.doi.org/10.1007/978-981-15-4756-0{_}50.

[6] B.M.M. Bomani, CubeSat Technology Past and Present: Current State-of-the-Art Survey, Tech. Rep., National Aeronautics and Space Administration, 2021, URL http://www.sti.nasa.gov.

[7] C. Clark, Clark SSC10-III-5 Huge Power Demand...Itsy-Bitsy Satellite: Solving the CubeSat Power Paradox, Tech. Rep..

[8] NASA, What is a DiskSat?, URL https://www.nasa.gov/smallspacecraft/disksat/.

[9] The Aerospace Corporation, DiskSat: Think outside the box, URL https://aerospace.org/disksat.

[10] R.P. Welle, C.C. Venturini, D.A. Hinkley, J.W. Gangestad, The DiskSat: A Two-Dimensional Containerized Satellite, Tech. Rep..

[11] R. Welle, C. Venturini, D. Hinkley, J. Gangestad, S. Grasso, A. Muszynski, R. Hunter, C. Frost, D. Mayer, C. Baker, DiskSat: Demonstration Mission for a Two-Dimensional Satellite Architecture, Tech. Rep..

[12] N.H. Crisp, P.C. Roberts, S. Livadiotti, V.T. Oiko, S. Edmondson, S.J. Haigh, C. Huyton, L.A. Sinpetru, K.L. Smith, S.D. Worrall, J. Becedas, R.M. Domínguez, D. González, V. Hanessian, A. Mø lgaard, J. Nielsen, M. Bisgaard, Y.A. Chan, S. Fasoulas, G.H. Herdrich, F. Romano, C. Traub, D. García-Almiñana, S. Rodríguez-Donaire, M. Sureda, D. Kataria, R. Outlaw, B. Belkouchi, A. Conte, J.S. Perez, R. Villain, B. Heißerer, A. Schwalber, The benefits of very low earth orbit for earth observation missions, Prog. Aerosp. Sci. 117 (2020) http://dx.doi.org/10.1016/j.paerosci.2020.100619.

[13] N.H. Crisp, P.C. Roberts, F. Romano, K.L. Smith, V.T. Oiko, V. Sulliotti-Linner, V. Hanessian, G.H. Herdrich, D. García-Almiñana, D. Kataria, S. Seminari, System modelling of very low Earth orbit satellites for Earth observation, Acta Astronaut. 187 (2021) 475–491, http://dx.doi.org/10.1016/j.actaastro.2021.07.004.

[14] ENPULSION, NanoFEEP Datasheet, Tech. Rep..

[15] R. Birkeland, CubeSat propulsion: Expanding the affordable space platform, 2018, (January).
[16] J. Hudson, S. Spangelo, A. Hine, D. Kolosa, K. Lemmer, Mission analysis for CubeSats with micropropulsion, J. Spacecr. Rockets 53 (5) (2016) 836–846, http://dx.doi.org/10.2514/1.A33564.
[17] I. Levchenko, K. Bazaka, Y. Ding, Y. Raitses, S. Mazouffre, T. Henning, P.J. Klar, S. Shinohara, J. Schein, L. Garrigues, M. Kim, D. Lev, F. Taccogna, R.W. Boswell, C. Charles, H. Koizumi, Y. Shen, C. Scharlemann, M. Keidar, S. Xu, Space micropropulsion systems for Cubesats and small satellites: From proximate targets to furthermost frontiers, Appl. Phys. Rev. 5 (1) (2018) http://dx.doi.org/10.1063/1.5007734.
[18] E. Dale, B. Jorns, A. Gallimore, Future directions for electric propulsion research, Aerospace 7 (9) (2020) http://dx.doi.org/10.3390/AEROSPACE7090120.
[19] S.H. Yeo, H. Ogawa, D. Kahnfeld, R. Schneider, Miniaturization perspectives of electrostatic propulsion for small spacecraft platforms, 2021, http://dx.doi.org/10.1016/j.paerosci.2021.100742.
[20] C.E. Pigeon, N.G. Orr, B.P. Larouche, V. Tarantini, G. Bonin, R.E. Zee, A Low Power Cylindrical Hall Thruster for Next Generation Microsatellites, Tech. Rep..
[21] G.C. Potrivitu, Y. Sun, M.W.A. bin Rohaizat, O. Cherkun, L. Xu, S. Huang, S. Xu, A review of low-power electric propulsion research at the space propulsion centre Singapore, 2020, http://dx.doi.org/10.3390/AEROSPACE7060067.
[22] T. Ikeda, K. Togawa, H. Tahara, Y. Watanabe, Performance characteristics of very low power cylindrical Hall thrusters for the nano-satellite "pROITERES-3", Vacuum 88 (1) (2013) 63–69, http://dx.doi.org/10.1016/j.vacuum.2012.04.012.
[23] A. Gurciullo, J. Jarrige, P. Lascombes, D. Packan, Experimental Performance and Plume Characterisation of a Miniaturised 50W Hall Thruster, Tech. Rep., 2019, URL https://hal.science/hal-02422774.
[24] D. Feili, B. Lotz, S. Bonnet, B.K. Meyer, H.W.L. Justus, N. Puetmann, μNRIT-2.5-A New Optimized Microthruster Of Giessen University, Tech. Rep..
[25] P.-Y.C.R. Taunay, S.G. Bilén, M.M. Micci, Numerical Simulations of a Miniature Microwave Ion Thruster, Tech. Rep..
[26] T.A. Trudel, S.G. Bilén, M.M. Micci, Design and Performance Testing of a 1-cm Miniature Radio-Frequency Ion Thruster, Tech. Rep..
[27] M.R. Natisin, H.L. Zamora, W.A. McGehee, N.I. Arnold, Z.A. Holley, M.R. Holmes, D. Eckhardt, Fabrication and characterization of a fully conventionally machined, high-performance porous-media electrospray thruster, J. Micromech. Microeng. 30 (11) (2020) http://dx.doi.org/10.1088/1361-6439/abb8c3.
[28] D. Bock, M. Tajmar, Highly miniaturized FEEP propulsion system (NanoFEEP) for attitude and orbit control of CubeSats, Acta Astronaut. 144 (2018) 422–428, http://dx.doi.org/10.1016/j.actaastro.2018.01.012.
[29] D. Bock, M. Tajmar, D. Bock, M. Bethge, M. Tajmar, Highly Miniaturized FEEP Thrusters for CubeSat Applications, Tech. Rep., 2014.
[30] S. Hurley, G. Teel, J. Lukas, S. Haque, M. Keidar, C. Dinelli, J. Kang, Thruster Subsystem for the United States Naval Academy's (USNA) Ballistically Reinforced Communication Satellite (BRICSat-P), Tech. Rep. ists30, 2016.
[31] S. Ciaralli, M. Coletti, S.B. Gabriel, Results of the qualification test campaign of a Pulsed Plasma Thruster for Cubesat Propulsion (PPTCUP), Acta Astronaut. 121 (2016) 314–322, http://dx.doi.org/10.1016/j.actaastro.2015.08.016.
[32] M. Coletti, F. Guarducci, S.B. Gabriel, A micro PPT for Cubesat application: Design and preliminary experimental results, Acta Astronaut. 69 (3–4) (2011) 200–208, http://dx.doi.org/10.1016/j.actaastro.2011.03.008.
[33] F. Rysanek, J.W. Hartmann, J. Schein, R. Binder, SSC02-I-2 MicroVacuum Arc Thruster Design for a CubeSat Class Satellite, Tech. Rep..
[34] J. Saletes, K. Saddul, A. Wittig, M. Kim, Implementation of direct battery driven discharge in triggerless operation of vacuum arc thrusters, J. Electr. Propuls. 3 (1) (2024) 4, http://dx.doi.org/10.1007/s44205-023-00065-8.
[35] K. Saddul, J. Saletes, M. Kim, A. Wittig, Mission analysis of a 1U CubeSat post-mission disposal using a thin-film vacuum arc thruster, Acta Astronaut. 219 (2024) 318–328, http://dx.doi.org/10.1016/j.actaastro.2024.03.019.
[36] J.E. Polk, M.J. Sekerak, J.K. Ziemer, J. Schein, N. Qi, A. Anders, A theoretical analysis of vacuum arc thruster and vacuum arc ion thruster performance, IEEE Trans. Plasma Sci. 36 (5 PART 1) (2008) 2167–2179, http://dx.doi.org/10.1109/TPS.2008.2004374.
[37] J. Saletes, M. Kim, K. Saddul, A. Wittig, K. Honda, P. Katila, Development of a Novel CubeSat De-Orbiting All Printed Propulsion System, Tech. Rep., 2022.
[38] E. Friedman, Erich's Packing Center, URL https://erich-friedman.github.io/packing/.
[39] G.E. Reis, Dense Packing of Equal Circles within a Circle, Tech. Rep. 1, 1975, pp. 33–37.
[40] R.L. Graham, B.D. Lubachevsky, K.J. Nurmela, P.R.J. Östergård, Discrete Dense packings of congruent circles in a circle, Tech. Rep., 1998, pp. 139–154.
[41] O. Montenbruck, Satellite Orbits, Springer, 2000.
[42] NASA Goddard Space Flight Center, General Mission Analysis Tool (GMAT) Mathematical Specifications, Tech. Rep., 2020.
[43] L.H. Sentman, Free Molecule Flow Theory and Its Application to the Determination of Aerodynamic Forces, Lockheed Aircraft Corporation, 1961.
[44] E.K. Sutton, Effects of Solar Disturbances on the Thermosphere Densities and Winds from CHAMP and GRACE Satellite Accelerometer Data, Tech. Rep., 2008.
[45] S. Frey, C. Colombo, S. Lemmens, Extension of the King-Hele orbit contraction method for accurate, semi-analytical propagation of non-circular orbits, Adv. Space Res. 64 (1) (2019) 1–17, http://dx.doi.org/10.1016/j.asr.2019.03.016.
[46] F. Landis Markley, J.L. Crassidis, Fundamentals of Spacecraft Attitude Determination and Control.
[47] D.A. Vallado, Fundamentals of Astrodynamics and Applications, Microcosm Press, 2013.
[48] H. Curtis, Orbital Mechanics for Engineering students, Elsevier, 2005.